




# Multiscale Analysis of the Gold Dust Defect in AISI 430 Industrial Stainless Steels: Influence of the Aluminum Content

BEATRIZ AMAYA DOLORES,<sup>1</sup> ILSE LETOFSKY-PAPST,<sup>2</sup>  
MANUEL DOMÍNGUEZ,<sup>3</sup> ANDRÉS NÚÑEZ GALINDO,<sup>4</sup>  
JOSÉ JUAN CALVINO GÁMEZ,<sup>1</sup> JUAN FRANCISCO ALMAGRO,<sup>4,5</sup>  
and LUC LAJAUNIE <sup>1,6</sup>

1.—Department of Materials Science and Metallurgical Engineering and Inorganic Chemistry, IMEYMAT, Faculty of Science, University of Cadiz, 11510 Puerto Real, Spain. 2.—Institute of Electron Microscopy and Nanoanalysis (FELMI) and Center for Electron Microscopy (ZFE), Graz University of Technology, NAWI Graz, Steyrergasse 17, 8010 Graz, Austria. 3.—Department of Condensed Matter Physics, IMEYMAT, Faculty of Science, University of Cadiz, 11510 Puerto Real, Spain. 4.—Laboratory and Research Section, Technical Department, Acerinox Europa S.A.U., 11379 Palmones, Spain. 5.—e-mail: juan.almagro@acerinox.com. 6.—e-mail: luc.lajaunie@uca.es

The “Gold Dust Defect” affects the surface quality of AISI 430 ferritic stainless steels. However, there is a very limited number of studies focusing on it. To better understand its nature, we have combined several techniques, such as x-ray photoelectron spectroscopy, atomic force microscopy, and transmission electron microscopy, in order to extract a maximum of structural and compositional information. Our results show that the surface quality, microstructure, and chemistry of the samples are strongly affected by the aluminum content, the severity of the defect being the highest at the lowest Al concentration. Not only is the concentration of the defects at the surface strongly reduced when increasing the Al. at.% but the depth of the cavities is also reduced by a factor of 3 when the Al content is increased from 0.09 at.% to 0.59 at.%. Our results provide new information on the nature of this defect, and show that an increase of the aluminum content allows the Cr concentration to be maintained in the range of values required to maintain the passivity of the steel, thus improving the surface quality.

## INTRODUCTION

Ferritic stainless steels (FSS) are used in a wide range of applications, including cutlery and washing machine drums, as well in the automotive and construction industries.<sup>1</sup> FSS offer an interesting balance between a competitive price and good physical, chemical, and mechanical properties, including an excellent resistance to stress corrosion cracking.<sup>2–4</sup> However, the production of FSS, in particular of AISI 430, is not completely controlled. In particular, they tend to present a surface defect called the ‘Gold Dust Defect’ (GDD) which corresponds to flakes that detach from the surface of the

material and leave cavities in the surface.<sup>5</sup> The GDD gives to the material an impaired and sparkling appearance that detracts from its sale. At the industrial level, the tape test is used to observe the damage caused by GDD with the naked eye. Once the tape is removed, the asperities of the surface can be observed and the severity of the GDD can be appreciated (Fig. 1). The presence of the GDD obliges the manufacturer to develop additional control steps, which increase the final price and decompensate the advantage of using FSS. Despite this, there is an extremely limited number of studies focused on the GDD. It has been shown that chromium carbides precipitation accompanies the formation of the GDD, which means that it might be related to the tendency of FSS to be ‘sensitized’, i.e., to increase the susceptibility to intergranular corrosion.<sup>5</sup> Sensitization usually occurs at grain

(Received March 20, 2022; accepted August 23, 2022;  
published online September 8, 2022)

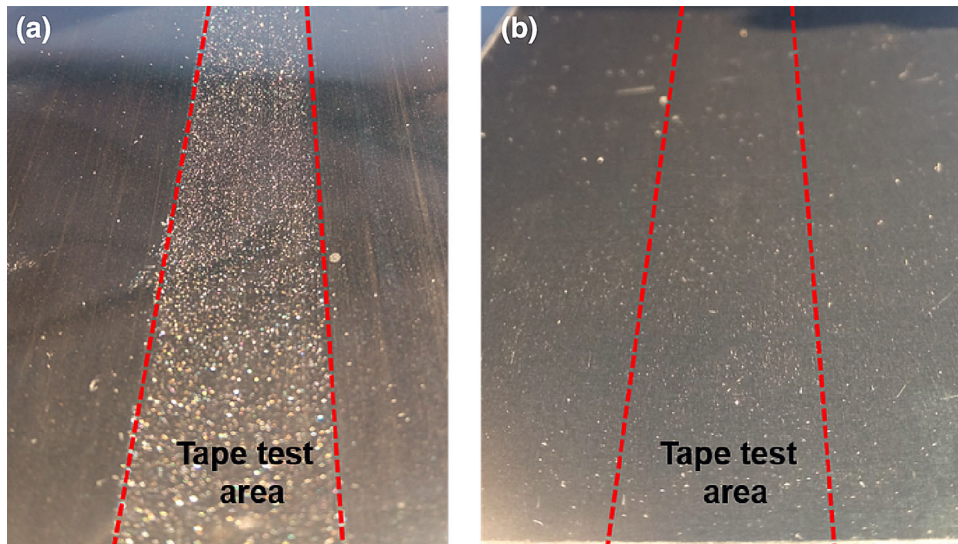


Fig. 1. (a) Sample with high GDD damages observed after the test tape. (b) Sample with low GDD damages observed after the test tape. The samples with high and low damage correspond to the samples Al1 and Al4 of this study, respectively.

boundaries, because they provide diffusion paths to nucleation sites for the precipitation of secondary phases, such as chromium carbides  $M_{23}C_6$  ( $Fe_{0.5}Cr_{0.5})_{23}C_6$ .<sup>6</sup> It induces a decrease of the chromium concentration in the areas adjacent to the carbides by about 9–10%, when compared to the ferritic matrix,<sup>7,8</sup> moving away the Cr concentration from the values which are required to maintain the passivity of the steel, and consequently leading to further deterioration.<sup>9</sup> It is known that the steps of the AISI 430 production process, where high temperatures are required, become crucial when studying sensitization, due to the precipitation of different phases, such as chromium carbides and carbonitrides.<sup>10–12</sup> Using alloying elements such as aluminum, which are more susceptible than chromium to form carbides, carbonitrides, and oxides, can mitigate the sensitization.<sup>13</sup>

To further explore the possible link between the GDD and sensitization, we have studied the influence of the aluminum content on the severity of the GDD in AISI 430 FSS. For this purpose, we have combined several techniques, including x-ray photoelectron spectroscopy (XPS), atomic force microscopy (AFM), scanning electron microscopy (SEM), and transmission electron microscopy (TEM), in order to extract a wealth of structural and compositional information. In particular, the TEM samples were prepared by using a focused ion-beam microscope (FIB), in order to be able to select the exact locations at the surface of the stainless steel sheets which were affected by the GDD.

## EXPERIMENTAL

### Materials

The AISI 430 ferritic stainless steel samples were cast at the Acerinox Europa facilities in the Bay of

Algeciras (Spain). These samples have gone through the same production process, in which the most important steps are constituted by a preheating in a furnace and then the hot-rolling process, in which the original thickness decreases from 200 mm to about 3.5 mm. Subsequently, the plates underwent annealing treatment to regenerate the ferritic microstructure. To further reduce the thickness of the steel, they went through the cold-rolling line to reach a final thickness of about 0.5 mm. Finally, the stainless steel plates were subjected to a final annealing treatment, called bright annealing, in order to remove possible internal structural alterations produced during the rolling process, and to give to the plates a bright finish. It was carried out in a reducing atmosphere composed of 75%  $H_2$  and 25%  $N_2$ , and at a temperature of 900°C, which was maintained during 20 min. Four different grades of FSS AISI 430 with different Al contents were used. Their raw compositions were obtained by x-ray fluorescence (XRF) and spark optical emission spectroscopy (S-OES) at the final stage of the production process at the factory, and are listed in Table I. The samples present an increase in Al content from 0.09% to 0.59 at.%. Furthermore, the tape tests carried out in the factory show that the sample with the lowest Al content (Al1) shows the highest GDD damage, while the sample with the highest Al content (Al4) shows the lowest GDD damage (cf. Fig. 1). The samples Al2 and Al3 show an intermediate behavior. It should be noted that Al2, Al3, and Al4 present similar Cu at.%, which allows us to decorelate the effect of the GDD from the Cu content.

### Physical Characterization Techniques

XPS analyses were performed by using a Kratos Axis UltraDL spectrometer (Kratos Analytical,

**Table I. Chemical composition obtained by XRF and S-OES (wt.% and at.%)**

Element	Al1		Al2		Al3		Al4	
	wt.%	at.%	wt.%	at.%	wt.%	at.%	wt.%	at.%
C	0.07	0.31	0.07	0.33	0.07	0.32	0.07	0.32
Cr	16.66	17.52	16.67	17.50	16.77	17.59	16.61	17.39
Mn	0.42	0.42	0.56	0.56	0.47	0.46	0.50	0.50
Si	0.47	0.92	0.50	0.97	0.54	1.05	0.54	1.04
Al	0.05	0.09	0.06	0.13	0.10	0.20	0.29	0.59
N	0.07	0.28	0.08	0.31	0.08	0.31	0.07	0.29
Cu	0.48	0.41	0.12	0.10	0.11	0.09	0.11	0.09
Fe	81.78	80.05	81.94	80.11	81.87	79.98	81.81	79.78

Manchester, UK), using a monochromatized Al K $\alpha$  ( $h\nu = 1486.6$  eV) source. The working power was 150 W and the vacuum condition in the analysis chamber was  $3 \times 10^{-9}$  Torr. High-resolution spectra were acquired with a pass energy of 20 eV in fixed analyzer transmission mode. The samples were placed in a sample holder by means of conductive double-sided carbon polymer tape. The binding energy scale was corrected with respect to the position of adventitious carbon (284.8 eV).<sup>14</sup> The oxidation states of Al, Fe, Cr, Mn, and Si were determined by the deconvolution of the 2p $_{3/2}$  lines.<sup>15,16</sup> AFM measurements were performed by using a Bruker Dimension ICON microscope in PeakForce Tapping mode, and by using a Bruker ScanAsyst-Air-type probe. The topographic data and corresponding 3D representations of the topography images were processed by using the Gwyddion software.

TEM samples were prepared by using a dual beam microscope FIB/SEM FEI Nova200 (Institute of Microscopy and Nanoanalysis of Graz, Technological University, Austria) equipped with an accelerated gallium ion gun and a platinum deposition system. The secondary electron image resolution at the dual beam coincidence point is 1.5 nm at 15 kV. The FIB optics have better than 7 nm resolution at 30 kV. For all the TEM samples, areas that included the GDD were selected (shown in supplementary Fig. S-1 in the Electronic Supplementary Material), and layers of Pt and C were deposited at the surface of the sample to protect it from ion damage.

TEM analyses were performed using a FEI Talos F200X microscope operated at 200 kV. This microscope is equipped with a high brightness field emission gun and a high-sensitivity energy dispersive x-ray spectroscopy (EDS) detection system (Chemi-STEM G2 Technology) that integrates 4 SDD detectors around the sample. The lamellas were analyzed by using high-resolution TEM (HR-TEM), spatially-resolved EDS, and a high-angle annular dark-field (HAADF) detector in scanning mode (STEM). EDS quantification was performed using the Brown-Powell cross-sections in the Velox software. The EDS resolution of the microscope is

equal to 136 eV at the Mn-K- $\alpha$  line. Cu-K lines arising from the TEM sample holder were deconvoluted prior to quantification. Due to the proximity between Cr-L and O-K lines, the Cr-K lines were used for chromium quantification. It should be noted that the Mn content could not be accurately quantified because of the overlap between the Mn-K- $\alpha$  line (5.89 keV) and the Cr-K- $\beta$  line (5.95 keV) on the one hand, and the overlap between the Mn-K- $\beta$  line (6.49 keV) and the Fe-K- $\alpha$  line (6.40 keV) on the other hand. Interpretation of the fast Fourier transform (FFT) patterns obtained from the HR-TEM images was performed using the Eje-Z software.

## RESULTS

### Surface Characterizations

Supplementary Fig. S-2 shows the XPS spectra acquired for the four samples. Several lines can be clearly observed, including those belonging to Al, Si, N, O, Cr, Mn, and Fe. In particular, an intense O 1s line can be observed for all the samples. The corresponding atomic compositions extracted from these spectra are shown in supplementary Table S-I. As expected, it is clear that the surface compositions determined by XPS are completely different from the matrix composition determined by XRF and S-OE. XPS analyses of stainless steels such as AISI 430 usually show the presence of a passive oxide layer, formed by Fe-Cr oxides, with an increasing Cr/Fe ratio towards the oxide/metal interface.<sup>17</sup> In the case of the sample which is the most affected by the GDD (Al1), the areas probed by XPS can be expected to be a complex mixture between the passive layer and the areas that have been affected by the GDD. Therefore, the composition determined by XPS for the sample whose surface is less affected by the GDD (Al4) should be closer to the composition of the passive layer.

According to the results of the low-resolution XPS spectra (supplementary Table S-I), the sample with the highest Al content (Al4) shows the lowest chromium content (about 5 at.% and 7 at.% for the rest of the samples, respectively) and the highest

aluminum content (about 18 at.%). On the other hand, the samples Al2 and Al3 show similar Al surface contents (10 at.%), whereas no Al is detected at the surface of the Al1 sample. In addition, all the samples show the presence of approximately 60% oxygen, which can be attributed to the presence of surface oxides, the concentration being slightly higher for the Al1 sample (about 69 at.% and 58 at.% for the rest of the samples).

The analyses of the high-resolution Al 2p spectra are shown in Fig. 2a. It should be noted that, because of the low at.% of Al for the Al1 sample, accurate analysis of the Al 2p edge was not possible. The remaining samples present a low concentration of metallic Al (about 2%). The main contribution for the Al4 sample corresponds to  $\text{Al}_2\text{O}_3$  (about 60%), whereas, for both the Al2 and Al3 samples, the main contribution comes from  $\text{Al}(\text{OH})_3$  (about 55% and 63%, respectively). The analyses of the high-resolution O 1s spectra are shown in Fig. 2b. The O 1s region presents a double peak for the Al1, Al2, and Al3 samples, which can be ascribed to the presence of metal oxides and metal carbonates<sup>16</sup> in similar proportions for the three samples. For the Al4 sample, the main contribution comes from the presence of metal oxides (about 80%), transforming the double peak into a well-defined of O 1s peak. Figure 2c shows the high-resolution spectrum of the Cr 2p edge. The main components can be attributed to the presence of metallic Cr,  $\text{Cr}_2\text{O}_3$  and  $\text{Cr}(\text{OH})_3$ .<sup>18</sup>

The presence of  $\text{Cr}(\text{OH})_3$  could result from the reaction of oxygen from air and/or water with the initial chromium oxides. The Al1 sample shows the lowest contribution of  $\text{Cr}^0$  and  $\text{Cr}(\text{OH})_3$  and the highest contribution of  $\text{Cr}_2\text{O}_3$ . On the other hand, the Al4 sample shows the highest contribution of  $\text{Cr}^0$  and  $\text{Cr}(\text{OH})_3$  and the lowest contribution of  $\text{Cr}_2\text{O}_3$ . The samples Al2 and Al3 both present an intermediate behavior. Analyses of the high-resolution Fe 2p XPS spectra are shown in Fig. 2d. The behavior of the samples Al1 and Al4 is once again completely different. For Al1, the Fe 2p main component corresponds to FeO, with a minority contribution from  $\text{Fe}^0$ ,<sup>16</sup> while the main contribution for Al4 comes from  $\text{Fe}^0$  with a small contribution from FeO. A similar behavior is observed for the Al2 and Al3 samples. In addition, Mn 2p and Si 2p high-resolution spectra were also acquired and analyzed, and are discussed in the Supplementary Fig. S-3. The quantification of the high-resolution XPS spectra are shown in Table II.

In summary, the composition and the chemical nature of the surfaces probed by XPS show strong variations as a function of the Al content. In particular, the sample with the highest Al content (Al4) presents a higher concentration of metallic Cr, metallic Fe, and  $\text{Al}_2\text{O}_3$ . The surface being richer in aluminum oxides rather than chromium and iron oxides, it allows Fe and Cr to remain in their metallic state, thus helping to mitigate

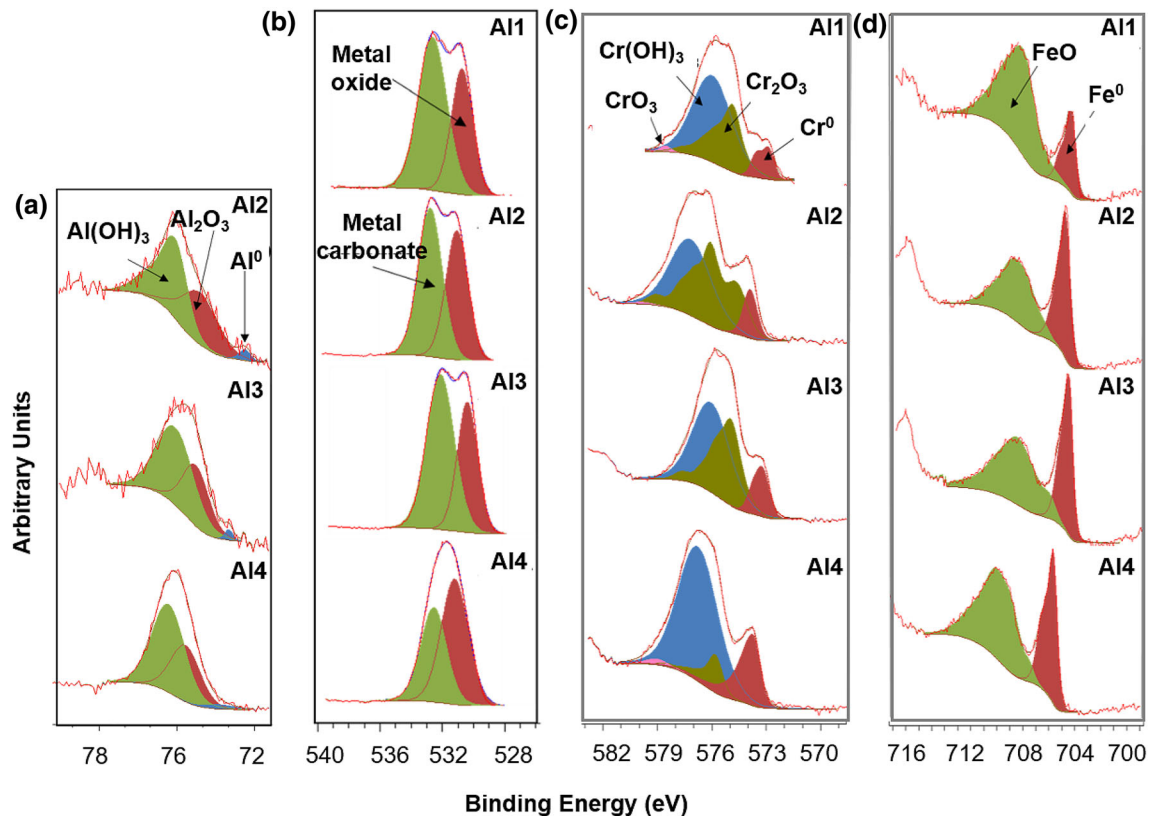


Fig. 2. High-resolution XPS spectra acquired in the vicinity of the: (a) Al 2p and (b) O 1s, (c) Cr 2p and (d) Fe 2p lines.



sensitization. On the other hand, the surface of the sample with the lowest Al content (Al4) shows contributions coming mainly from FeO and Cr<sub>2</sub>O<sub>3</sub>, thus preventing the steel from maintaining its passivity.

Figures 3 and 4, and supplementary Figs. S-4 and S-5, show the SEM micrographs acquired on the Al1, Al2, Al3 and Al4 samples in different areas before and after the tape test. Before the tape test, the surface of the Al1 sample presents a higher density of defects than the other samples. The density of the flakes has been estimated from the SEM images, and is equal to  $6.2 \times 10^{-4} \pm 0.6$  flakes/ $\mu\text{m}^2$ ,  $5.1 \times 10^{-4} \pm 0.7$  flakes/ $\mu\text{m}^2$ ,  $4.5 \times 10^{-4} \pm 0.6$  flakes/ $\mu\text{m}^2$ , and  $1.4 \times 10^{-4} \pm 0.4$  flakes/ $\mu\text{m}^2$

for the Al1, Al2, Al3, and Al4 samples, respectively. The Al content seems to lead to a decrease in the density of the defects present at the surface of the samples. Figure 4 shows the SEM micrographs acquired at higher magnifications. The size of the flakes also seems to be dependent on the Al content, and they present larger dimensions for the Al1 samples than for the other samples. The typical dimensions are equal to  $226 (\pm 41) \times 42 (\pm 9) \mu\text{m}$ ,  $87 (\pm 6) \times 21 (\pm 8) \mu\text{m}$ ,  $68 (\pm 8) \times 24 (\pm 7) \mu\text{m}$ , and  $44 (\pm 6) \times 19 (\pm 2) \mu\text{m}$  for the Al1, Al2, Al3, and Al4 samples, respectively. In addition, after the tape test, the surface of the Al1 sample shows the presence of flakes that are almost completely detached from the surface. In the case of Al4, there is hardly any difference between before and after the tape test, and the flakes seems to adhere better to the surface.

**Table II. High-resolution XPS spectra quantification of Al1, Al2, Al3, and Al4 for Al 2p, Cr 2p, Fe 2p, and O 1s**

Region	Compound	Al1	Al2	Al3	Al4
Al 2p	Al (0)	–	2.9	1.9	1.6
	Al <sub>2</sub> O <sub>3</sub>	–	42.3	35.5	60.1
	Al(OH) <sub>3</sub>	–	54.8	62.6	38.3
Cr 2p	Cr <sup>0</sup>	5.5	9.6	12.6	21.3
	Cr <sub>2</sub> O <sub>3</sub>	62.7	47.0	38.4	9.9
	Cr(OH) <sub>3</sub>	31.2	42.9	49.0	67.3
	CrO <sub>3</sub>	0.6	0.5	0	1.5
Fe 2p	Fe <sup>0</sup>	22.4	74.3	68.3	62.6
	FeO	77.6	25.7	31.7	37.4
O 1s	Metal oxides	38.1	44.6	38.3	83.7
	Metal carbonates	61.9	55.4	61.7	16.3

Figure 5 shows the 3D representations of the topography of the AFM images for the samples Al1 and Al4. It should be noted that the AFM images were acquired at the lowest scan size ( $50 \times 50 \mu\text{m}$ ) allowed by the microscope. The presence of cracks can be observed in the surface of both samples. In the case of Al1 (Fig. 5a and b), the average depth of the cracks is about  $0.75 \mu\text{m}$  and can reach up to  $1.25 \mu\text{m}$ . For this sample, the entire length of the cracks exceeds the lowest scan size that can be acquired by the microscope, in good agreement with the SEM observations. On the other hand, the average depth for the Al4 sample (Fig. 5c and d) is about  $0.25 \mu\text{m}$ . The length of the cracks for Al4 is about  $20 \mu\text{m}$ . The analyses were repeated on

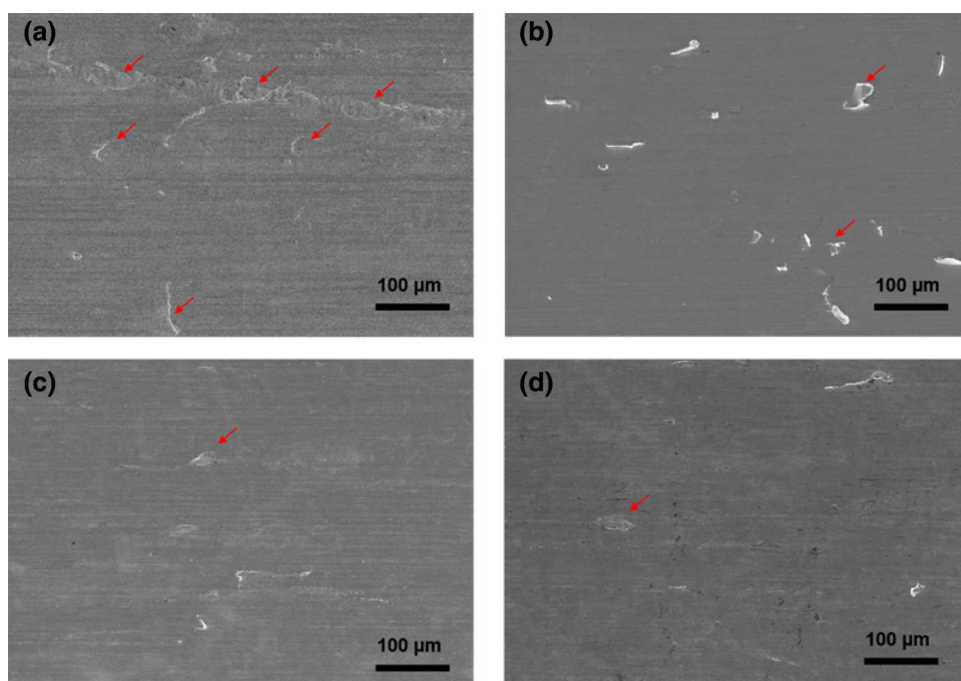


Fig. 3. Low-magnification SEM images of: (a) Al1 before the tape test, (b) Al1 after the tape test, (c) Al4 before the tape test, and (d) Al4 after the tape test. The red arrows highlight the presence of the GDD (Color figure online).

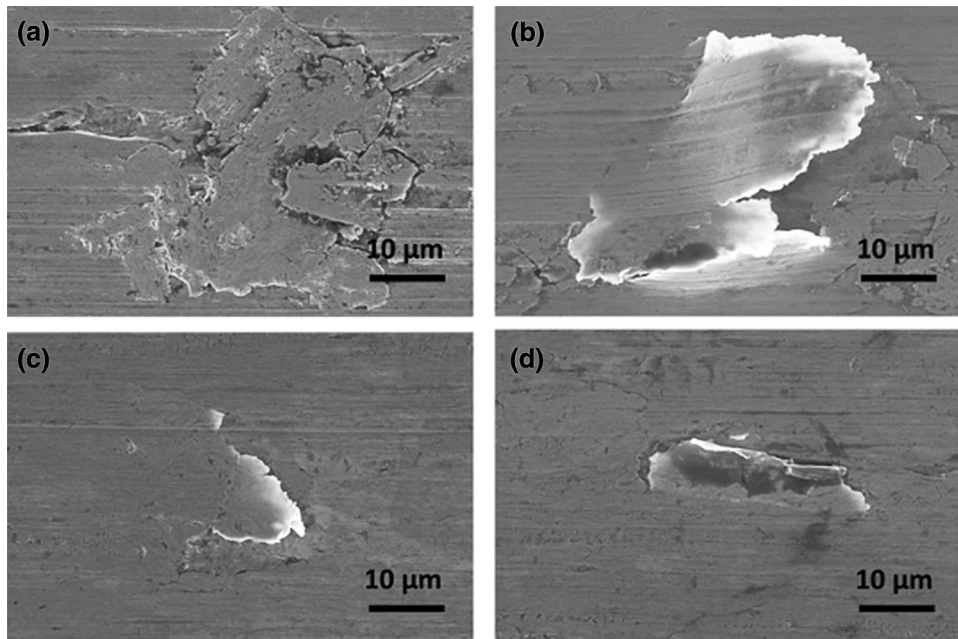


Fig. 4. Medium-magnification SEM images of: (a) Al1 before the tape test, (b) Al1 after the tape test, (c) Al4 before the tape test, and (d) Al4 after the tape test.

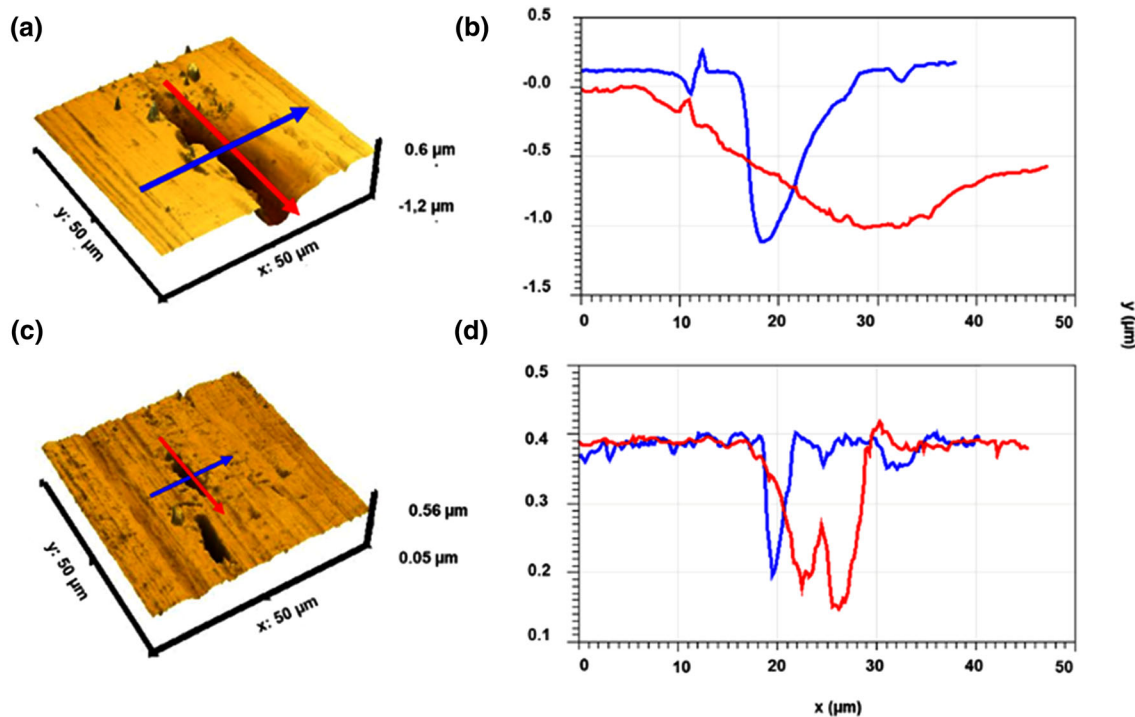


Fig. 5. (a) 3D representation of the topography images of the Al1 sample. The red and blue arrows highlight the area used to extract the (b) corresponding depth profiles of the Al1 sample ( $\mu\text{m}$ ). (c) 3D representation of the topography images of the Al4 sample. The red and blue arrows highlight the area used to extract the (d) corresponding depth profiles of the Al4 sample ( $\mu\text{m}$ ) (Color figure online).

various cracks, and confirmed that, for the Al4 sample, the depth of the cracks is reduced by roughly a factor of 3, when compared to the Al1 sample. The SEM and AFM results show that the

aluminum content of the matrix has a strong influence on the quality of the surface. In particular, the sample with the highest aluminum content (Al4) presents a surface which is less altered by the GDD

than the sample with the lowest aluminum content (Al1).

**(S)TEM Analyses**

Figure 6 shows the (S)TEM micrographs acquired on the sample Al1 prepared in cross-section. Above the surface of the samples, two layers rich in Pt and C were deposited at the surface of the sample during the sample preparation by FIB. A discontinuous top layer, with a maximum thickness of about 700 nm, can be observed at the surface of the sample. The discontinuity of the top layer can be explained by the detachment of the flakes from the surface, as observed by SEM. The grains of the top layer present a columnar growth, have a size of about  $100 \times 200$  nm, and show variations of diffraction contrast in the corresponding TEM image (Fig. 6b). These grains are much smaller than the grains of the FSS matrix that have a dimension of about  $5 \mu\text{m}$  and more. The presence of smaller grains with a columnar growth was also observed in the case of deep drawing and welds, in which grain coarsening

occurs in the heat area and deep drawing areas.<sup>19,20</sup> Fig. 7 shows the STEM-EDS analysis of the Al1 sample. The presence of continuous cracks separating the top layer from the FSS matrix can be clearly observed, as well as cracks inside the top layer. The outer diameter of the cracks is typically around 10–20 nm. The grains A, B, and C (as labeled in Fig. 6b) were studied by EDS, and the corresponding EDS spectra are shown in Fig. 7b. In addition, areas labeled D and E in Fig. 7a were selected as reference for the top layer and the stainless steel matrix, respectively. The presence of oxygen and nitrogen is observed (both in the EDS spectra and in the EDS chemical maps (Fig. 7b and c) in grain C. The quantifications of the Cr and Fe elements extracted from the EDS spectrum are shown in supplementary Table S-II. The FSS matrix presents a Cr at.% of about 18% with a Cr/Fe ratio equal to 0.2. Grains A, B, and C present higher Cr at.% values, with a Cr/Fe ratio ranging from 0.7 to 12.6. In particular, grain C presents the highest at.% of Cr ( $\sim 93\%$ ), with a Cr/Fe ratio of 12.6. With respect to the FSS

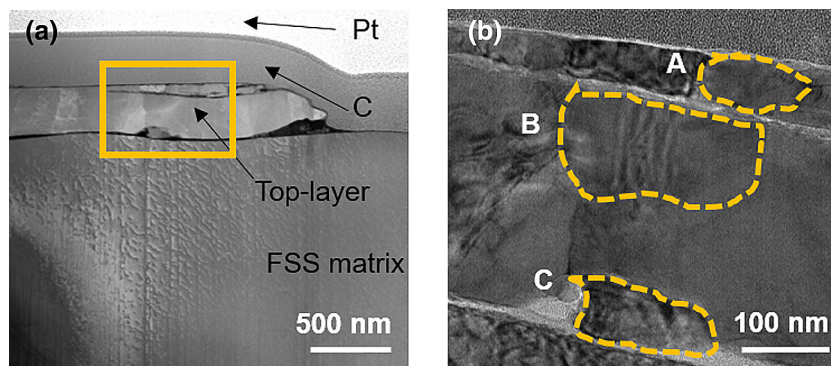


Fig. 6. (S)TEM micrographs of Al1: (a) STEM-HAADF micrograph of the Al1 sample prepared in cross-section. The yellow rectangle highlights the area shown at higher magnification in (b) TEM micrograph of the enlarged area of the top layer. The grains labelled A, B, and C have been selected for further analyses shown in Figs. 7 and 8 (Color figure online).

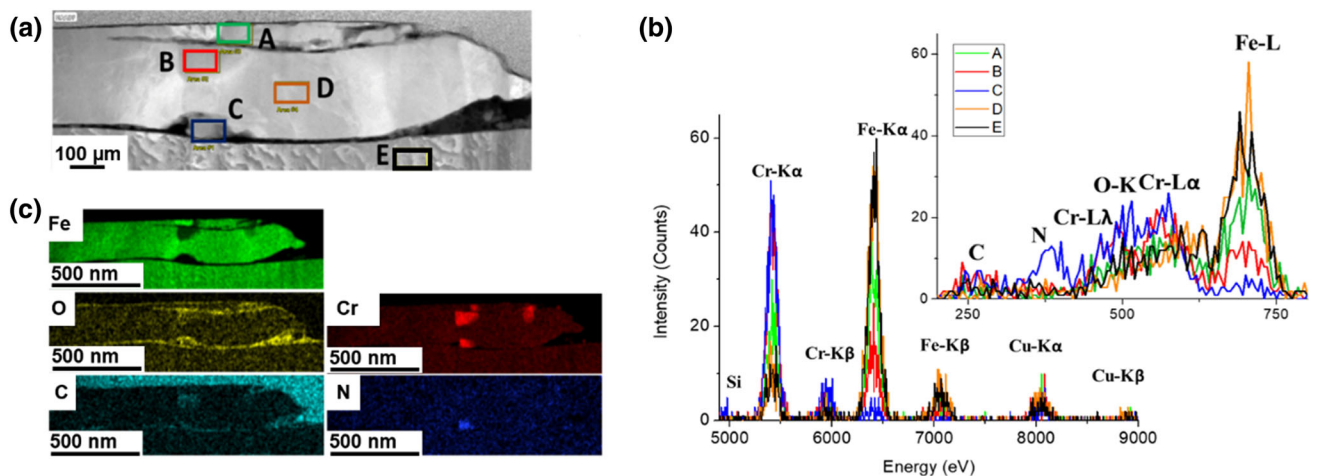


Fig. 7. STEM-EDS analyses of the Al1 sample: (a) STEM-HAADF micrograph. The rectangles labeled A, B, C, D, and E correspond to the area used to extract the corresponding spectra. (b) EDS spectrum. The inset shows the low-energy range of the spectra. (c) Corresponding EDS chemical maps.



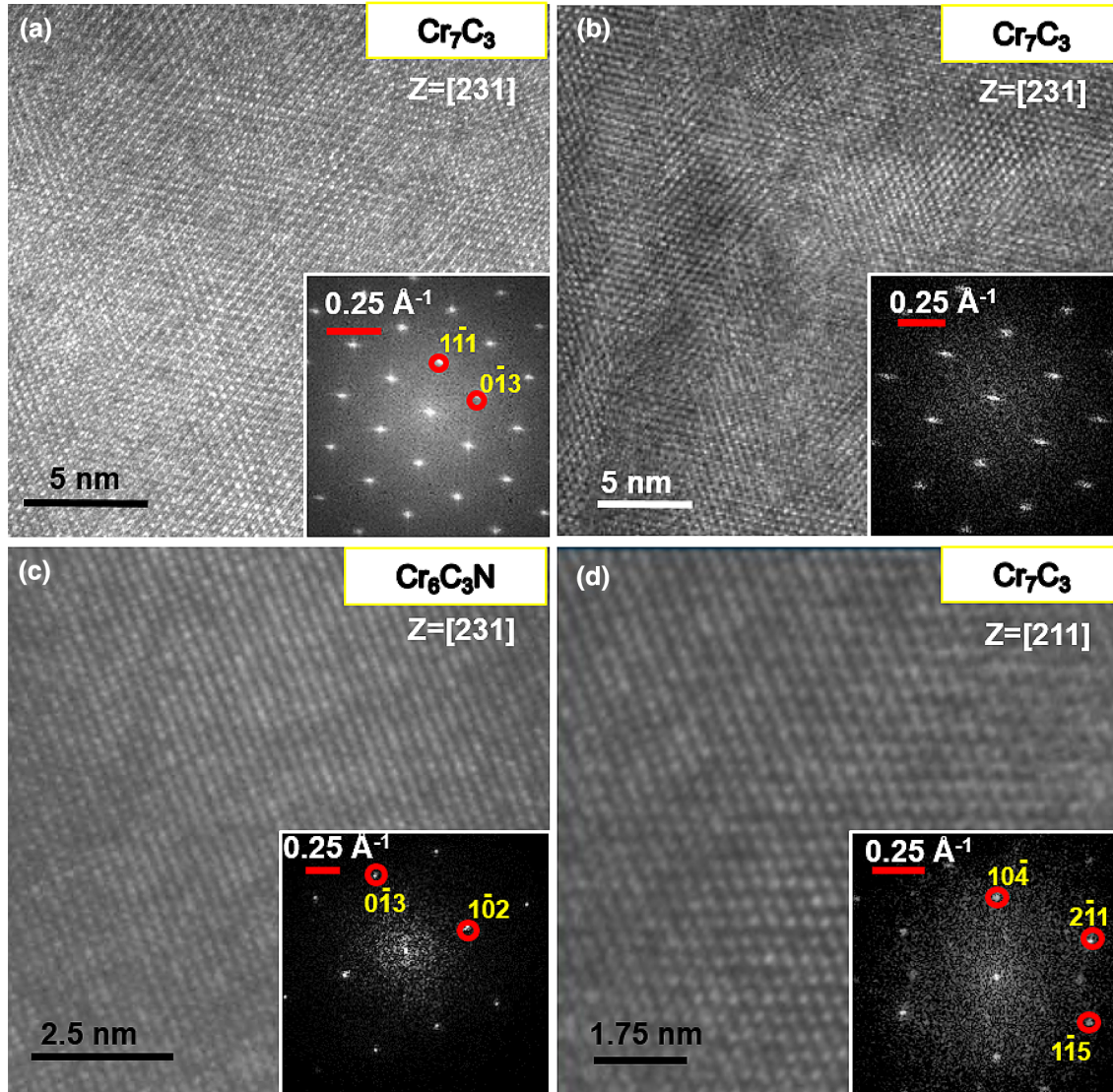


Fig. 8. HR-TEM micrographs and corresponding FFT patterns acquired on the Al1 sample on the corresponding grains: (a) grain A, (b) grain B, (c d) grain C of the top-layer of the Al1 sample, as labeled in Fig. 6b.

matrix (area labeled as E in Fig. 7a), the rest of the top layer (area D) presents values similar to the FSS matrix with slightly higher and lower values of Cr at.% and Fe at.% by about 2 at.%, respectively. It should be noted that no Al signal was evidenced in the EDS spectrum, which means that the Al content in this probed area is below the EDS detection limit.

Figure 8 shows high-resolution TEM images of the grains A, B, and C with their respective FFT patterns. The crystalline nature of the top layer can be clearly highlighted from the HR-TEM micrographs. It is important to note that grains A and B (Fig. 8a and b) show unambiguous FFT patterns that can both be indexed as corresponding to the hexagonal crystal system  $\text{Cr}_7\text{C}_3$  ( $\text{M}_7\text{C}_3$ ) with the space group P63mc crystal structure. The chromium carbide  $\text{Cr}_7\text{C}_3$  is considered a metastable carbide and was already observed in welded areas of FSS.<sup>21</sup>

It has been shown that, when increasing the temperature,  $\text{M}_3\text{C}$  precipitates first followed by  $\text{M}_7\text{C}_3$  and, finally,  $\text{M}_{23}\text{C}_6$ .<sup>22,23</sup> For grain C (Fig. 8c and d), it shows mostly overlapping crystalline phases. Small crystalline domains of about 20 nm have been found corresponding to the  $\text{Cr}_6\text{C}_3\text{N}$  phase (Fig. 8c). In addition, even smaller crystalline domains (around 5 nm) have been found corresponding to the  $\text{Cr}_7\text{C}_3$  phase (Fig. 8d).

Figure 9 shows the STEM micrograph acquired on the sample Al4 prepared in cross-section. For this sample, the presence of a top layer separated from the FSS matrix by cracks can also be observed. Grains smaller than those in the FSS matrix are also observed in the top layer. It should be noted that the presence of a top layer was also observed for Al2 and Al3 (not shown here). It has a thickness of about 900 nm, and, contrary to what have been



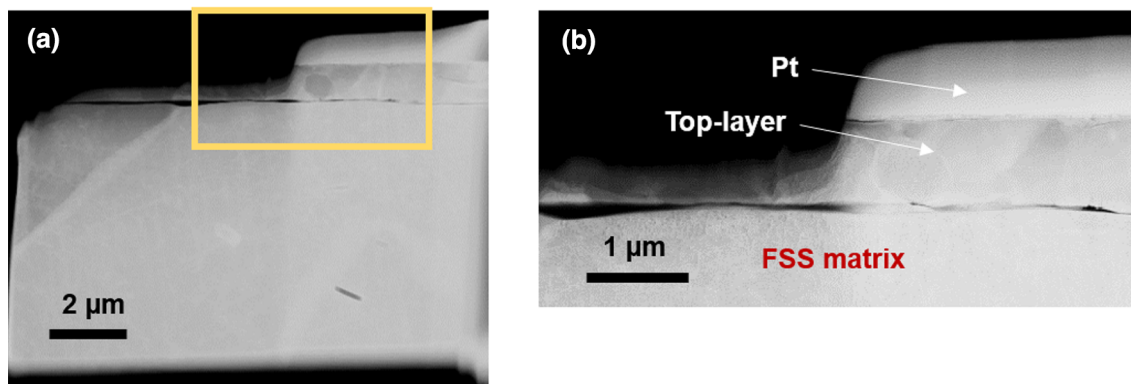


Fig. 9. STEM-HAADF micrograph of the Al4 sample prepared in cross-section: (a) at 2  $\mu\text{m}$  and (b) at 1  $\mu\text{m}$  scale.

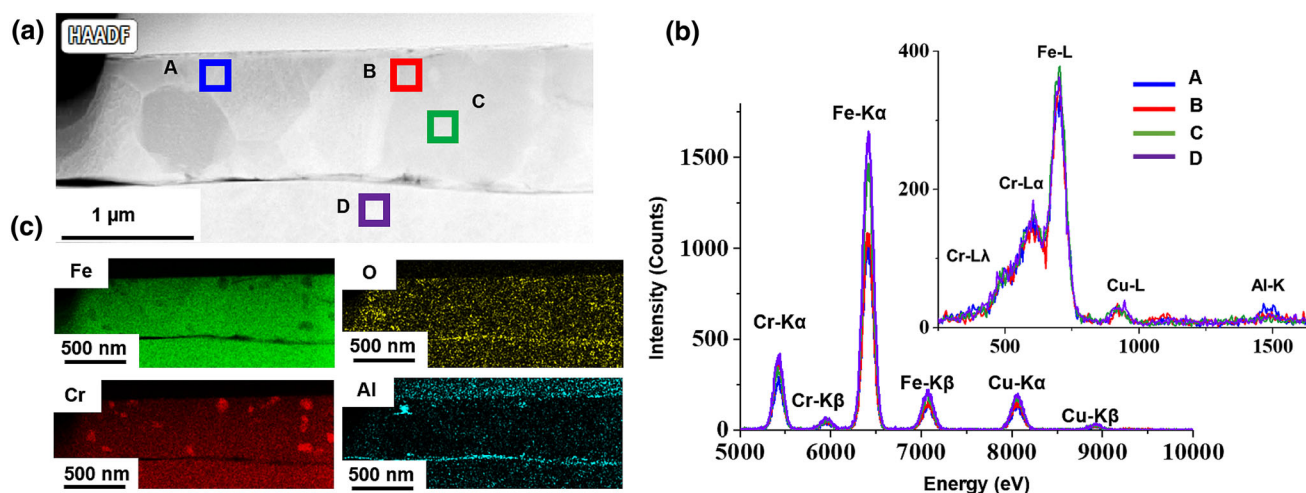


Fig. 10. STEM-EDS analyses of the Al4 sample: (a) STEM-HAADF micrograph. The rectangles labeled A, B, C, and D correspond to the area used to extract the corresponding spectra. (b) EDS spectra. The inset shows the low-energy range of the spectra. (c) Corresponding EDS chemical maps.

observed for Al1, the top layer does not show any discontinuity. Figure 10 shows the STEM-EDS analyses of the Al4 sample. The corresponding chemical compositions are given in supplementary Table S-III. It should be noted that no C and N signals were highlighted in the probed area. As already observed for the Al1 sample, grains corresponding to Cr accumulation and Fe deficiency are also present. For areas A, C, and D, the Fe/Cr ratio is between 4.2 and 4.6. However, the precipitate with Cr accumulation has a ratio of 3.3, corresponding to a Cr increase of about 5 at.% compared to the FSS matrix. Furthermore, the Cr content in the top layer is decreased by about 1 at.% compared to the matrix content. A small precipitate rich in Al (1.2 at.% Al) is also observed, with dimensions of about  $250 \times 220$  nm. In addition, contrary to the rest of the samples, a passive layer rich in O, Al, and Cr is also observed. The results of the STEM-EDS analysis for the surface of the Al4 sample is shown in

supplementary Fig. S-6. A passive layer with a thickness of 15 nm that is rich in O (18 at.%), Cr, (71 at.%), and Al (11 at.%) is observed at the surface of the sample. On the other hand, the Fe content is decreased by about 20 at.% compared to the stainless steel matrix.

## CONCLUSION

We have studied the influence of the aluminum content on the severity of the “Gold Dust Defect” (GDD) in AISI 430 ferritic stainless steels with a bright annealed finish. Our results show that the quality of the surface, the microstructure, and chemistry are strongly affected by the aluminum content. In particular, the density of defects at the surface is reduced by a factor 4.4 when the Al content is increased from 0.09 at.% to 0.59 at.%. The depth of the cavities is also reduced by a factor of 3. In addition, all the samples show a singular

microstructure in which a top layer composed of smaller grains than those of the FSS matrix is observed at the surface of the sample. The presence of minority phases, such as  $\text{Cr}_7\text{C}_3$  and  $\text{Cr}_6\text{C}_3\text{N}$ , was also observed for the sample with the lowest Al content. All these results highlight how an increase of the Al content allows the maintaining of the Cr concentration in the range of values required to retain the passivity of the steel, thus improving the quality of the surface. However, even for the sample with the highest Al content, sub-surface defects can still be observed, and further research focusing on this complex defect is needed.

### ACKNOWLEDGEMENTS

The authors acknowledge funding from the Andalusian regional government (FEDER-UCA-18-106613), the European Union's Horizon 2020 research and innovation program (Grant Agreement 823717 – ESTEEM3) and the Spanish Ministerio de Economía y Competitividad (PID2019-107578GA-I00). The authors also acknowledge the use of (S)TEM instrumentation provided by the National Facility ELCMI ICTS (“División de Microscopía Electrónica”, Universidad de Cadiz, DME-UCA).

### FUNDING

Open Access funding provided thanks to the CRUE-CSIC agreement with Springer Nature.

### CONFLICT OF INTEREST

The authors declare that they have no conflict of interest.

### OPEN ACCESS

This article is licensed under a Creative Commons Attribution 4.0 International License, which permits use, sharing, adaptation, distribution and reproduction in any medium or format, as long as you give appropriate credit to the original author(s) and the source, provide a link to the Creative Commons licence, and indicate if changes were made. The images or other third party material in this article are included in the article's Creative Commons licence, unless indicated otherwise in a credit line to the material. If material is not included in the article's Creative Commons licence and your intended use is not permitted by statutory regulation or exceeds the permitted use, you will need to obtain permission directly from the copyright holder. To view a copy of this licence, visit <http://creativecommons.org/licenses/by/4.0/>.

### SUPPLEMENTARY INFORMATION

The online version contains supplementary material available at <https://doi.org/10.1007/s11837-022-05478-8>.

### REFERENCES

1. K.A. Cashell and N.R. Baddoo, *T. Struct.* 83, 169. <https://doi.org/10.1016/j.tws.2014.03.014> (2014).
2. M. Ryan, D. Williams, R. Chaler, B. Hutton, and D. McPhail, *Nat.* 415, 770. <https://doi.org/10.1038/415770a> (2002).
3. J. Charles, J.D. Mithieux, P.O. Santacreu, and L. Peguet, *Rev. Metall.* 106, 124. <https://doi.org/10.1051/metal/2009024> (2009).
4. M.O. Amuda, E. Akinlabi, and S. Mridha, *Ref. Modul. Mater. Sci. Mater. Eng.* <https://doi.org/10.1016/B978-0-12-803581-8.04010-8> (2016).
5. S. Mithra, P.G. Venkatakrishnan, D. Noorullah, and V. Karthik, *Int. Jour. Adv. Eng. Manag. Sci.* 3, 4. (2017).
6. E. Stanbury and R. Buchanan, *ASM Int.* <https://doi.org/10.4028/www.scientific.net/KEM.545.143> (2002).
7. G. Mallaiah, A. Kumarb, P. Ravinder Reddy, and G. Madhusudhan Reddy, *Mat. Des.* <https://doi.org/10.1016/j.matdes.2011.11.063> (2012).
8. M.O. Amuda and S. Mridha, *Int. J. Corr.* <https://doi.org/10.1155/2011/305793> (2011).
9. D. Balsaraf, S. Ambade, A. Patil, and Y. Puri, *Adv. Mat. Man. Char.* 3, 263. <https://doi.org/10.11127/ijammc.2013.02.048> (2013).
10. R.P. Siqueira, H.R. Sandim, T.R. Oliveira, and D. Raabe, *Mat. Sci. Eng. A.* 528, 3513. <https://doi.org/10.1016/j.msea.2011.01.007> (2011).
11. M. Masoumi, S. Tavares, J. Pardal, T. Martins, M. da Silva, and H. de Abreu, *Eng. Fail. Anal.* 79, 198. <https://doi.org/10.1016/J.ENGFAILANAL.2017.04.008> (2017).
12. M. Alizadeth, S.P.H. Marashi, and M. Pouranvari, *Mat. Des.* 56, 258. <https://doi.org/10.1016/j.matdes.2013.11.022> (2014).
13. W. Du, L. Jiang, Q. Sun, Z. Liu, and X. Zhang, *J. Iro. Ste. Res. Int.* 17, 47. [https://doi.org/10.1016/S1006-706X\(10\)60113-6](https://doi.org/10.1016/S1006-706X(10)60113-6) (2010).
14. A. Barroso, G. Blanco, J.J. Pérez, C. Escudero, E. Pellegrin, F.C. Herrera, and J.M. Pintado, *Mat.* 14, 711. <https://doi.org/10.3390/ma14040711> (2021).
15. M. Descostes, F. Mercier, N. Thromat, C. Beaucaire, and M. Gautier, *App. Surf. Sci.* 165, 288. [https://doi.org/10.1016/S0169-4332\(00\)00443-8](https://doi.org/10.1016/S0169-4332(00)00443-8) (2000).
16. M.C. Biesinger, B.P. Payne, L.W.M. Lau, A. Gerson, and R.S.C. Smart, *Surf. Int. Anal.* 41, 324. <https://doi.org/10.1002/SIA.3026> (2009).
17. C. Abreu, M. Cristóbal, R. Losada, X. Nóvoa, G. Pena, and M. Pérez, *Elec. Act.* 51, 2991. <https://doi.org/10.1016/j.electacta.2005.08.033> (2006).
18. A.M. Dayaghi, M. Askari, H. Rashtchi, and P. Gannon, *Surf. Coat. Tech.* 223, 110. <https://doi.org/10.1016/j.surfcoat.2013.02.041> (2013).
19. C. Tembhurkar, R. Kataria, S. Ambade, J. Verma, A. Sharma, and S. Sarkar, *Mat. Eng. Perf.* 30, 1444. <https://doi.org/10.1007/s11665-020-05395-4> (2021).
20. H.J. Shin, J.K. An, S.H. Park, and D.N. Lee, *Act. Mat.* 51, 4693. [https://doi.org/10.1016/S1359-6454\(03\)00187-3](https://doi.org/10.1016/S1359-6454(03)00187-3) (2003).
21. T. Teker, *Int. Jour. Adv. Man. Tech.* 69, 1833. <https://doi.org/10.1007/s00170-013-5158-8> (2013).
22. A. Bjärbo and M. Hättestrand, *Met. Mat. Trans. A.* 32, 19. <https://doi.org/10.1007/s11661-001-0247-y> (2001).
23. T. Fujita and N. Takashi, *Mat. Sci.* 18, 702. <https://doi.org/10.2355/isijinternational1966.18.702> (1978).

**Publisher's Note** Springer Nature remains neutral with regard to jurisdictional claims in published maps and institutional affiliations.